remote sensing

MDPI

Article

High Precision Motion Compensation THz-ISAR Imaging Algorithm Based on KT and ME-MN

Wei Liu, Hongqiang Wang *, Qi Yang, Bin Deng, Lei Fan and Jun Yi

College of Electronic Science, National University of Defense Technology, Changsha 410073, China; liuwei17@nudt.edu.cn (W.L.); yangqi08@nudt.edu.cn (Q.Y.); dengbin@nudt.edu.cn (B.D.); fanlei15@nudt.edu.cn (L.F.); yijun@nudt.edu.cn (J.Y.)

* Correspondence: wanghongqiang@nudt.edu.cn

Abstract: In recent years, terahertz (THz) radar has been widely researched for its high-resolution imaging. However, the traditional inverse synthetic aperture radar (ISAR) imaging algorithms in the microwave band perform unsatisfactorily in the THz band. Firstly, due to THz radar's large bandwidth and short wavelength, the rotation of the target will result in serious space-varying(SV) range migration and space-varying phase error. Furthermore, it is challenging to accurately estimate the rotational velocity and compensate for phase errors in the presence of severe range migration effects. Therefore, in this paper, a high-precision THz-ISAR imaging algorithm is proposed. The algorithm includes the following step: First, the SV first-order range migration(FRM) is corrected using keystone transform (KT); then, the minimum entropy based on modified newton (ME-MN) is used to estimate the rotational velocity roughly, and the remaining SV second-order range migration(SRM) is corrected to obtain the range profile with the envelope alignment. Finally, the echo after the envelope alignment is processed for the second time based on ME-MN. The target rotation velocity is accurately estimated, and the phase error is compensated to obtain a well-focused imaging result. The validity of the proposed method is verified by numerical simulation and electromagnetic calculation data.

Keywords: terahertz (THz) radar; inverse synthetic aperture radar (ISAR); newton method (NM); second-order range migration (SRM) correction; rotation estimation

Citation: Liu, W.; Wang, H.; Yang, Q.; Deng, B.; Fan, L.; Yi, J. High Precision Motion Compensation THz-ISAR Imaging Algorithm Based on KT and ME-MN. *Remote Sens.* **2023**, *15*, 4371. https://doi.org/10.3390/rs15184371

Academic Editors: Massimiliano Pieraccini, Junkun Yan, Xiaolong Li, Shisheng Guo, Chenguang Shi and Avik Santra

Received: 11 July 2023
Revised: 16 August 2023
Accepted: 31 August 2023
Published: 5 September 2023

1. Introduction

ISAR emits electromagnetic waves to obtain high-resolution two-dimensional images of non-cooperative targets in all-day, all-weather conditions, offering critical support for target recognition [1]. Therefore, it can be applied in military and civilian [2,3]. At present, ISAR imaging technology is widely used in the microwave band. However, the microwave band radar is limited by the bandwidth, resulting in low imaging resolution and low recognition rate. By contrast, the THz radar owns the higher carrier frequency and the more extensive bandwidth to achieve high-resolution imaging by the shorter observation time [4,5].

THz wave is also called a sub-millimeter wave, and its frequency range from 0.1 THz~10 THz. At the same time, some of the characteristics of microwave and infrared, are due to the THz wave between the microwave and infrared band. In the early stage, limited by the hardware such as the THz Source design, the range, and field of view of THz radar are severely limited. Therefore, THz radar was mainly used for near-field imaging and measuring THz targets' scattering characteristics. [6–8]. With the advancement of technology, THz radar is gradually developing in the SAR / ISAR imaging field. In 2012, the UESTC successfully implemented a 220 GHz terahertz radar imaging system based on solid-state electronic sources. It used this system to perform ISAR imaging experiments on aircraft target models [9]. In the same year, to further apply THz radar technology to longer-range detection and to take advantage of its high frame rate imaging

characteristics, DARPA launched the Video Synthetic Aperture Radar (ViSAR) project. The ViSAR project successfully built a one-transmitter four-receiver terahertz radar system. It obtained high-resolution and high-frame rate SAR images of ground-moving targets at a range of 4 km through experiments in 2017 [10]. This result confirmed the feasibility of terahertz radar for long-range applications. In 2022, Emidio Marchetti et al. from the University of Birmingham in the United Kingdom proposed the concept of spaceborne sub-THz-ISAR space situational awareness. In space, the range of THz radar is no longer restricted by atmospheric absorption. At the same time, terahertz waves can sense diffuse echoes from rough surfaces of extended targets due to their short wavelength. Terahertz radar can achieve the ultra-high resolution of less than 1 cm, allowing the inversion of the fine structure of space targets due to its high carrier frequency and large bandwidth. These characteristics of THz radar give it significant advantages and potential for the component-level recognition and interpretation of ISAR images of space targets [11–13].

Although THz radar has the potential to generate ISAR images with high-precision, high-resolution, and high frame rates, it also puts forward higher requirements for imaging processing algorithms. The conventional ISAR imaging process mainly consists of envelope alignment and initial phase correction. Researchers have proposed several methods for these two imaging steps to refine the ISAR imaging technique further. Currently, two main approaches are usually used to achieve envelope alignment: the cross-correlation method and the alignment criterion based on image quality [14,15]. After the envelope alignment is completed, the range units of each echo are aligned, but the initial phase correction is needed before the final imaging. Research related to initial phase error correction in the microwave band is well established. Such algorithms are divided into two main categories: the first one is based on the dominant scatterer and the second one is based on image quality. The first class of algorithms is based on the main scatterer algorithm which first selects the main scatterer by a criterion such as minimum variance, and compensates for the initial phase by using the phase of the strong scattering point as a reference. Relevant algorithms include the dominant scatterer algorithm (DSA) and phase gradient algorithm (PGA) [16,17]. The second class of algorithms is based on global image quality optimization. The initial phase error of the echo is compensated through iterative optimization by selecting image quality criteria such as image entropy, image contrast, and image sharpness. Such algorithms include the minimum entropy algorithm (MEA) [18] and the maximum contrast algorithm (MCA) [19].

The traditional two-step compensation method can no longer meet the demand for high-resolution imaging to obtain a focused ISAR image. The range offset and phase error generated during rotational motion will seriously affect the ISAR imaging quality. Moreover, the range offset and phase error are high-order quantities that cannot be corrected by traditional motion compensation algorithms. Therefore, KT is proposed to solve the FRM. The algorithm realizes frequency resampling by linear interpolation and can remove the FRM without parameters [20].

In this way, the rotation-induced range offset is eliminated. However, in practical processing, the second-order space-varying range migration generated by the increased resolution of terahertz radar can no longer be ignored, which is rarely considered in conventional frequency bands [21]. After the range migration correction is completed, the high-order space-varying phase error introduced by rotation will lead to Doppler broadening, and this broadening phenomenon becomes particularly serious due to the short THz wavelength. Compensation for higher-order space-varying phase errors must estimate the rotational parameters of the target, such as rotation velocity and rotation center.

The estimation of the rotational parameters algorithm is mainly divided into two categories: image-driven and data-driven. Among them, the image-driven algorithm directly estimates the rotation angle of two ISAR images by matching the images and then calculates the target rotational velocity, but the error is large. The second class of data-driven algorithms is also divided into two, one is based on parameter estimation, where the quadratic

phase coefficients of the strong scattering points in the one-dimensional range profile are estimated by means of parameter estimation, and then fitted to obtain the target's rotation velocity and rotation center. This algorithm requires multiple strong scattering points and good alignment of the range profile envelope. Another algorithm is based on the image quality criterion. However, terahertz radar is unable to ignore the effect of second-order range offsets, which will severely affect the estimation of rotational speed. Another algorithm is based on image quality criteria. This type of algorithm uses the rotation velocity and the rotation center of the required solution, constructs a phase compensation matrix and uses the image quality as an optimization criterion to finally obtain the rotational parameters of the required solution. This type of algorithm is robust but also requires a one-dimensional range profile envelope to be well aligned. Outside, a rotational velocity estimation method is proposed based on maximizing the envelope sharpness. Since a quantitative relationship exists between the second-order range bending and the rotational velocity, the correct rotational velocity can be obtained when the range profile envelope sharpness is maximized by correcting the SRM using the rotational velocity. However, this method fails at low SNR and the accuracy of the resulting rotational velocity is not high. And the algorithm subsequently needs to estimate the center of rotation to compensate for the phase error [21]. Therefore, achieving high-order space-varying phase compensation and high-accuracy rotational parameters estimation in the presence of severe second-order space-varying range migration remains a challenging problem.

To solve the above problems, a THz-ISAR processing flow and algorithm are proposed in this paper. Firstly, the KT is performed on the echo signal after the translation compensation to correct the first-order space-varying range migration. Combined with the ME-MN, the rotation velocity and center are preliminarily estimated. Because the requirement for range migration correction accuracy is related to the range resolution, while the requirement for phase error compensation accuracy is related to the wavelength [22]. The first estimated rotation velocity corrects the second-order space-varying range migration, and the range profile envelope has been aligned. Finally, the first estimated rotation velocity and center are taken as the initial values, and the ME-MN is used again for the echo after the SRM correction to perform accurate parameter estimation and phase error compensation. The main contributions of this paper are as follows:

1. The influence of range migration and phase error caused is analyzed in the terahertz band. It shows that THz-ISAR imaging must consider the second-order space-varying range migration correction problem.
2. The ME-MN is used to accurately estimate the target's rotation velocity and center to achieve second-order space-varying range migration correction and second-order space-varying phase compensation. Two iterations of the algorithm give more accurate results and allow parameters such as rotation velocity and center to be solved. In addition, azimuthal scaling of the target can be achieved using the estimated rotation velocity
3. A modified Newton method is used to modify the step size and the Hessian matrix, avoiding the problem that the Newton method fails when the Hessian matrix is not positive. At the same time, the method also enables fast estimation of the rotational parameters.

This paper is arranged as follows: Section 2 introduces the THz-ISAR signal model, and the influence of range migration and phase error on imaging is analyzed. Section 3 gives the THz-ISAR imaging process and the derivation of the proposed method. In Section 4, the effectiveness of the proposed algorithm is verified by the simulation and the electromagnetic calculation. Section 5 gives a conclusion and future research directions.

2. THz-ISAR Signal Model

Because THz-ISAR is suitable for applications in space, the object considered is the space target. As shown in Figure 1, in the geometric model of THz-ISAR imaging, the target moves from A to B. According to the far-field assumption, the motion process is

decomposed into three parts. Firstly, point A is translated to point C along the radar line of sight. In this process, all scattering points move the same, and the generated Doppler is the same, so it is called translation. Secondly, at point C, the target rotates around the center of rotation. Because of the rotation, the range from different scattering points to the radar varies inconsistently. The generated Doppler can be used to distinguish different scattering points and provide azimuth resolution. Finally, the target moves in a circular motion from C to B with the radar at its center. During this process, all scattering points remain at the same distance from the radar, which does not affect the imaging results. Therefore, Thus, the motion of the target with respect to the radar can be independently decomposed into translational and rotational components. Considering the initial slant distance and the instantaneous change in slant distance due to translational motion, the slant range $R_i(t_m)$ of scattering point i can be expressed as

$$R_i(t_m) \quad = r_0 + r(t_m) + x_i \sin \omega t_m + y_i \cos \omega t_m \tag{1}$$

where t_m is the slow time, r_0 is the initial slant range, and r_m is the slant range of the target rotation center changing with the slow time. Assuming that the radar transmits a linear frequency modulation (LFM) signal:

$$s(\hat{t}; t_m) \quad = \text{rect}\left[\frac{\hat{t}}{T_p}\right] \cdot \exp\left(j2\pi f_c t + j\pi\gamma \hat{t}^2\right) \tag{2}$$

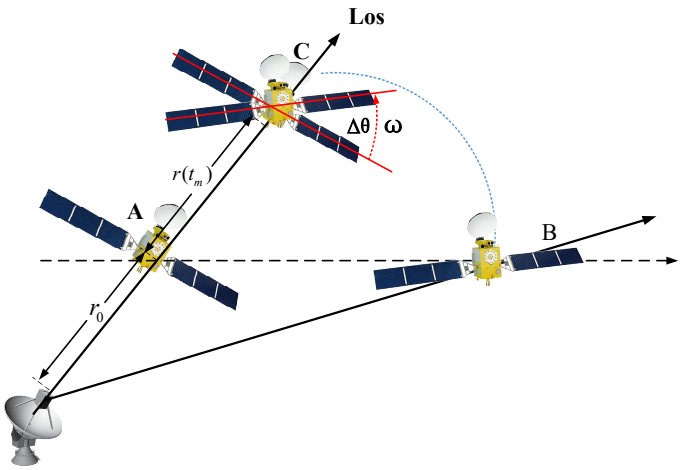

Figure 1. THz-ISAR imaging geometric model of space target.

After the time delay

$$\tau = \frac{2R_i(t_m)}{c} \tag{3}$$

the obtained echo signal is

$$s_i(\hat{t}; t_m) = \text{rect}\left[\frac{\hat{t} - 2R_i(t_m)/c}{T_p}\right] \cdot \exp\left\{j2\pi f_c\left[\hat{t} - \frac{2R_i(t_m)}{c}\right] + j\pi\gamma\left[\hat{t} - \frac{2R_i(t_m)}{c}\right]^2\right\} \tag{4}$$

where T_p is the pulse width, f_c is the carrier frequency, and γ is the frequency modulation of the LFM signal. Perform dechirp and pulse compression on the echo signal:

$$S(f_r; t_m) = \sum_{i=0}^{Q-1}\left\{\sigma_i \cdot \text{sinc}\left\{T_p\left[f_r + \frac{2R_i(t_m)}{c}\right]\right\} \cdot \exp\left[-j\frac{4\pi f_c}{c}R_i(t_m)\right]\right\} \tag{5}$$

The above echoes are compensated for translation to remove the phase and migration effects produced by $r_0 + r(t_m)$, the echoes can be expressed as:

$$S(f_r; t_m) = \sum_{i=1}^{Q} \left\{ \sigma_i \cdot \mathrm{sinc}\left\{ T_p \left[f_r + \frac{x_i \sin \omega t_m + y_i \cos \omega t_m}{c} \right] \right\} \right\} \cdot \exp\left[-j \frac{4\pi f_c}{c} (x_i \sin \omega t_m + y_i \cos \omega t_m) \right] \tag{6}$$

After the translation compensation, the effect of migration and phase errors on imaging in the THz bands will be quantitatively analyzed below. The trigonometric function in Equation (6) is Taylor expanded as follows:

$$\begin{cases} \sin \omega t_m \approx \omega t_m - \frac{1}{6} \omega^3 t_m^3 \\ \cos \omega t_m \approx 1 - \frac{1}{2} \omega^2 t_m^2 \end{cases} \tag{7}$$

Each term in Equation (7) produces range migration and phase error. The literature [23] states that when the following inequalities hold, the effect of the corresponding terms on the range migration and phase error is negligible.

$$\begin{cases} \Delta\theta D_a < \rho_r \\ \frac{1}{6} \Delta\theta^3 D_a < \rho_r \\ \frac{1}{2} \Delta\theta^2 D_r < \rho_r \\ \frac{2\pi f_c}{3c} \Delta\theta^3 D_a < \frac{\pi}{4} \\ \frac{2\pi f_c}{c} \Delta\theta^2 D_r < \frac{\pi}{4} \end{cases} \tag{8}$$

where $\Delta\theta$ is the accumulation angle of imaging, D_r and D_a are the maximum size of target range-dimension and azimuth-dimension respectively, and $\rho_r = c/2B$ is the range resolution. The above equation describes the range migration and phase error caused by rotation. In Equation (8), $\Delta\theta D_a$ and $\frac{1}{2}\Delta\theta^2 D_r$ are the FRM and the SRM, respectively. And the third-order range migration (TRM) $\frac{1}{6}\Delta\theta^3 D_a$ can usually be ignored, which will also be obtained later in the analysis. When the migration momentum exceeds the distance resolving unit, it leads to the defocusing of the range dimension. $\frac{2\pi f_c}{c}\Delta\theta^2 D_r$ and $\frac{2\pi f_c}{3c}\Delta\theta^3 D_a$ are range space-varying second-order phase error and azimuth space-varying third-order error, respectively. When two are greater than $\pi/4$, it will cause azimuth to defocus. The following numerical simulations are used to quantify the distance migration at different rotation angles, bandwidths and phase error at different rotation angles, and frequencies. Assuming that Da and Dr are 15 m, Figure 2 is the curve of the FRM, SRM and TRM with rotation angles under different bandwidths.

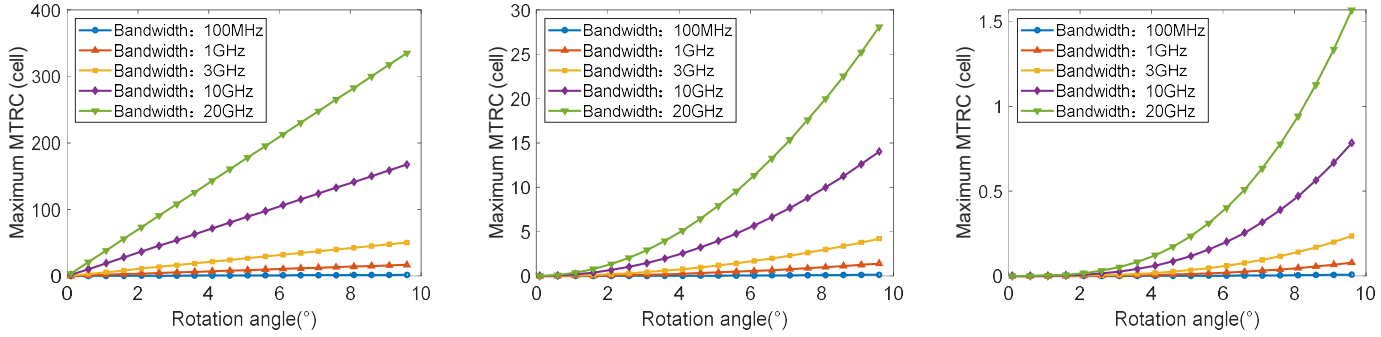

Figure 2. The range migration with rotation angles under different bandwidths. (**a**) The FRM; (**b**) the SRM; (**c**) the TRM.

Figure 2a shows that the FRM changes linearly with time. As the bandwidth increases, FRM must be considered. Figure 2b shows the variation curves of SRM with rotation angle under different bandwidths. From the diagram, we can see that with the increase in bandwidth, the SRM neglected in conventional radar must also be considered. Figure 2c is the TRM. Figure 3b shows that the TRM will not affect the imaging in most cases and can be generally ignored. As shown in Figure 3, we analyze the high-order phase errors generated by different carrier frequencies. Figure 3a,b are the second-order and third-order phase errors, respectively. In general, the third-order phase error is negligible for a limited target size and rotation angle. The results from Figure 2a show that the second-order phase error becomes larger as the carrier frequency increases. Figure 3c compares the azimuth profile with and without second-order phase error when the carrier frequency is 220 GHz, Dr = Da = 15 m, and the rotation angle is 5°. It can be illustrated that the second-order phase error in the THz band results in more severe azimuthal-defocusing compared to the conventional band. However, the severe azimuthal-defocus is favourable for the estimation of rotational parameters.

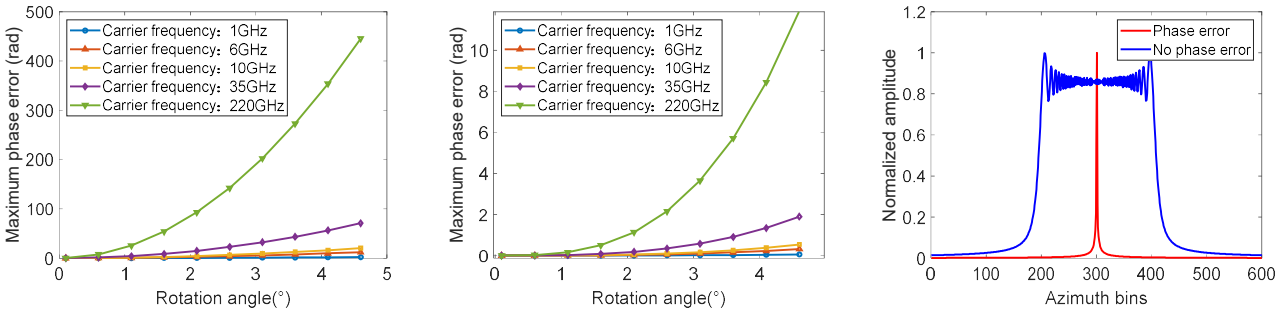

(**a**) (**b**) (**c**)

Figure 3. (**a**) The second-order SV phase error; (**b**) the third-order SV phase error; (**c**) the broadening of azimuth profile by the second-order phase error.

3. THz-ISAR Algorithm and Derivation

According to the analysis in Section 2, terahertz-ISAR imaging has a non-negligible SRM in addition to FRM. For the FRM, we can use KT to correct it. The correction of the SRM involves the rotational velocity. In addition, THz-ISAR has more serious second-order space-varying phase errors compared with microwave bands. Although the more serious phase error will bring a huge impact on the imaging, facilitates the estimation of the target rotational velocity. Similarly, under the influence of range migration, it is difficult to perform effective phase compensation for the unaligned envelope. To address the above problems, a THz-ISAR imaging method is proposed in this paper. The specific steps are as follows:

(1) KT is applied to remove the FRM of echoes after translational compensation.
(2) The ME-MN is used to estimate the rotation velocity and rotation center.
(3) Because the envelope alignment accuracy is comparable to the resolution, the SRM is corrected utilizing the rotational velocity information obtained in step (2) to obtain an aligned envelope. This process can be implemented using the Chirp-Z transform (CZT).
(4) The rotation velocity and center estimated in the second step are used as the initial values, and the ME-MN is used again for accurate parameter estimation of the envelope-aligned echoes. At the same time, cross-range scaling is implemented.
(5) Using the rotation parameters obtained in step 4, the phase compensation matrix is constructed, and the Fourier transform is performed along the azimuthal dimension after compensating for the echo. A well-focused THz-ISAR image is finally acquired.

The proposed processing flowchart is shown in Figure 4. Subsequent sections are specific to the implementation details of the proposed algorithmic process.

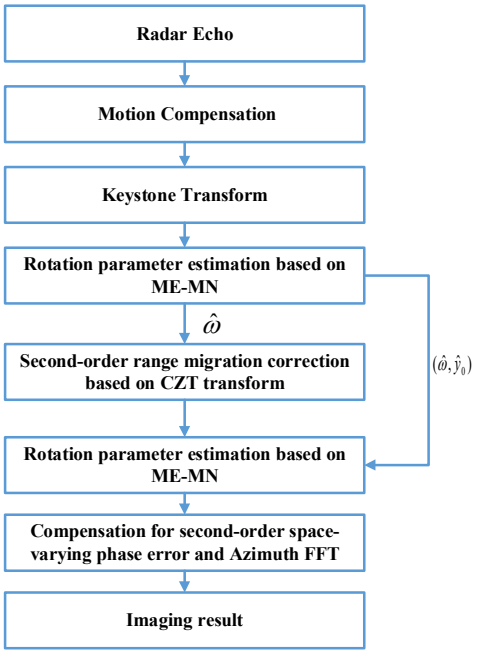

Figure 4. The proposed processing flowchart.

3.1. Correcting First-Order Range Migration by KT

Substituting Equation. (7) into Equation (6), after the range dimension IFFT transformation, Equation (5) is discretized to obtain

$$\begin{aligned} S(n;k) = \sum_{i=1}^{Q} \left\{ \sigma_i \cdot \exp\left[-j\tfrac{4\pi}{c}(n\Delta f_r + f_c) \cdot x_i \omega k \Delta t_m \right] \cdot \exp\left[-j\tfrac{4\pi}{c}(n\Delta f_r + f_c) \cdot y_i \right] \right\} \\ \cdot \exp\left[j\tfrac{2\pi}{c}(n\Delta f_r + f_c) \cdot y_i \omega^2 (k\Delta t_m)^2 \right] \end{aligned} \tag{9}$$

The KT, also known as keystone remapping, corrects linear range shifts in SAR/ISAR imaging by linearly interpolating to realign the time axis of each frequency cell with the expression

$$k\Delta t_m = \frac{f_c}{(n\Delta f_r + f_c)k'\Delta\tau_m} \tag{10}$$

Equation (9) is approximated by the KT as

$$\begin{aligned} S(n;k') = \sum_{i=1}^{Q} \sigma_i \cdot \exp\left[-j\tfrac{4\pi f_c}{c}\left(x_i \omega k' \Delta\tau_m - \tfrac{1}{2} y_i \omega^2 k'^2 \Delta\tau_m{}^2 \right) \right] \\ \cdot \exp\left[-j\tfrac{4\pi}{c} n\Delta f_r \cdot y_i (1 + \tfrac{1}{2}\omega^2 k'^2 \Delta\tau_m{}^2) \right] \end{aligned} \tag{11}$$

Converting Equation (10) to the range-frequency domain:

$$\begin{aligned} S(h;k') = \sum_{i=1}^{Q} \sigma_i \cdot \exp\left[-j\tfrac{4\pi f_c}{c}\left(x_i \omega k' \Delta\tau_m - \tfrac{1}{2} y_i \omega^2 k'^2 \Delta\tau_m{}^2 \right) \right] \\ \cdot \sin c\left\{ \left[h + \tfrac{2B}{c}(1 + \tfrac{1}{2}\omega^2 k'^2 \Delta\tau_m{}^2) y_i \right] \right\} \end{aligned} \tag{12}$$

In the above equation, the difference between terahertz radar and conventional band radar is the consideration of an additional term: $\frac{1}{2}\omega^2 k'^2 \Delta\tau_m{}^2$. This item leads to the SRM. And from the equation, it can be illustrated that the SRM is related to the rotation velocity and the coordinate: The larger the coordinate axis y_i is, the larger the range migration is, which shows the characteristic of space-varying, so it cannot be corrected uniformly as the translational compensation. And compensating for the SRM requires the acquisition of rotational velocity.

3.2. Rotation Estimation Based on ME-MN

From the analysis in Section 3.1, the rotational velocity must be estimated to calibrate the SRM. Therefore, this section will present a method for estimating the rotational velocity. The previous Section 1 describes methods for rotational velocity estimation, including image-based and data-based [24], and also explains the advantages and disadvantages of these methods. The image-based method mainly performs image rotation and matching to estimate the rotation angle by extracting strong scattering points in the image. This type of algorithm requires high image quality and requires multiple images. However, the imaging quality of terahertz radar can be severely degraded due to the second-order phase, leading to the failure of such methods. The second method is based on the data-driven method, which estimates the rotational velocity by estimating the quadratic phase coefficient in the signal. Azimuth frequency modulation estimation and iterative solutions based on image quality optimization are mainly used in practice. Azimuth frequency modulation estimation needs to select the range cell where the dominant scatterer is located, and the envelope needs to be completely aligned, so the robustness is weaker than the rotational velocity estimation method based on image quality. In this paper, the ME-MN is used to estimate the rotational velocity with the image entropy as the iterative optimization criterion. Image entropy (IE) is commonly used to measure the focusing performance of ISAR imaging. The smaller the IE value, the more well-focused the image is.

Assuming y_0 is the equivalent center of rotation, and the scattering points at the same range cell have the same y-coordinate, then $y_i = -\frac{c}{2B}h - y_0$. The echo $S(h;k')$ is multiplied by the phase-compensated term: $\exp(j\frac{2\pi f_c}{c}(\frac{c}{2B}h + y_0)\omega^2 {k'}^2 {\Delta\tau_m}^2)$. Finally, the azimuthal-dimensional FFT is applied to the phase-compensated echo to obtain the ISAR image $g(h;m;\mathbf{x})$:

$$g(n;m;\mathbf{x}) = \frac{1}{M}\sum_{k=M/2}^{M/2-1}\begin{bmatrix} S(n;k')\cdot\exp[jK\cdot(\frac{c}{2B}n + y_0)\cdot {k'}^2] \\ \exp(-j2\pi\frac{k'm}{M}) \end{bmatrix} \tag{13}$$

where let $\mathrm{x} = [K, y_0]^T$, $K = \frac{2\pi f_c}{c\cdot\Delta\tau_m^2}w^2$, The optimal parameters are obtained by minimizing the cost function:

$$\hat{\mathbf{x}} = \underset{\mathbf{x}}{\operatorname{argmin}}\{E_g(\mathbf{x})\} \tag{14}$$

In Equation (14), $\hat{\mathbf{x}}$ is the estimated value of $\mathbf{x}$, $E_g(\mathbf{x})$ is the IE of $g(h;m;\mathbf{x})$, which is defined as:

$$E_g(\mathbf{x}) = \ln E_g - \frac{1}{E_g}\sum_{n=-N/2}^{N2-1}\sum_{n=-M/2}^{M/2-1}\left[|g(n;m;\mathbf{x})|^2\cdot\ln|g(n;m;\mathbf{x})|^2\right] \tag{15}$$

In Equation (15), $E_g = \sum_{n=-N/2}^{N/2-1}\sum_{k=-M/2}^{M/2-1}\left|g(n;m;\mathbf{x})\right|^2$ represents the total energy of the image. The IE: E_g is independent of the phase error: $\exp(j\frac{2\pi f_c}{c}(\frac{c}{2B}h + y_0)\omega^2 {k'}^2 {\Delta\tau_m}^2)$, according to the Parseval theorem, so E_g is a constant.

The more effective methods for the above two-dimensional optimization problems are the gradient descent method(GDM) and the Newton method(NM). However, the traditional NM belongs to the unconstrained optimization problem and has the characteristics of fast convergence speed. In this paper, the NM is used to solve the optimization problem.

The gradient of the objective function to is

$$\nabla E = \left[\frac{\partial E}{\partial K}, \frac{\partial E}{\partial y_0}\right]^T \tag{16}$$

where

$$\frac{\partial E}{\partial K(y_0)} = -\frac{1}{E_g}\sum_{n=-N/2}^{N/2+1}\sum_{m=-M/2}^{M/2-1}\left[\left(1+\ln|g(n;m;\mathbf{x})|^2\right)\cdot\frac{d|g(n;m;\mathbf{x})|^2}{dK(y_0)}\right] \tag{17}$$

$$\frac{\partial|g(n;m;\mathbf{x})|^2}{\partial K(y_0)} = 2\mathrm{Re}[g^*(n;m;\mathbf{x})\cdot\frac{\partial g(n;m;\mathbf{x})}{\partial K(y_0)}] \tag{18}$$

The Hessian matrix of the cost function E_g in x is derived below

$$H = \begin{bmatrix} \frac{\partial^2 E}{\partial K^2} & \frac{\partial^2 E}{\partial K \partial y_O} \\ \frac{\partial^2 E}{\partial y_O \partial K} & \frac{\partial^2 E}{\partial y_O^2} \end{bmatrix} \tag{19}$$

In the above equation, $\frac{\partial^2 E}{\partial K \partial y_O} = \frac{\partial^2 E}{\partial y_O \partial K}$, so Hessian is a symmetric matrix. After obtaining the ∇E and Hessian matrix, the iterative equation can be expressed as

$$\mathbf{x}_{k+1} = \mathbf{x}_k - H_k^{-1}\nabla E_k \tag{20}$$

The above equation is the step of the traditional Newton iteration method. In the actual processing process, the IE of the imaging result has many local optimal points, as shown in Figure 5.

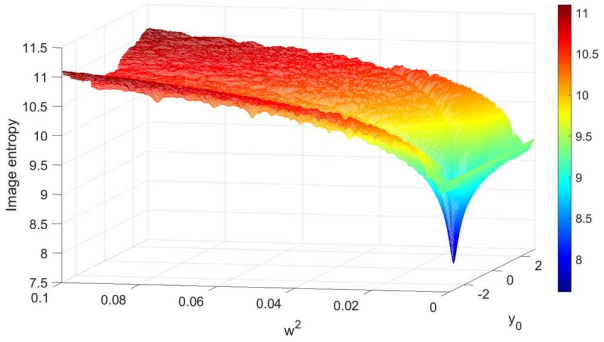

Figure 5. Two-dimensional image entropy.

At the same time, when the initial starting point is chosen far from the optimal solution, the Hessian matrix is not necessarily positive definite, which leads to the Hessian matrix not being invertible or the direction of the computed update being the direction that increases the objective function. At this moment, the NM fails, so the traditional NM should be modified and improved. The modified Newton method (MN) can be expressed as:

$$\mathbf{x}_{k+1} = \mathbf{x}_k - \lambda H'^{-1}_k \nabla E_k \tag{21}$$

Equation (21) contains two modifications to NM. The first is the step size factor. The step size coefficients can be used to prevent the objective function from falling into a local optimum by using a linear search method (e.g., the golden section method). Secondly, when the Hessian matrix is not positive, it is modified to be

$$H' = H + \mu I \tag{22}$$

where I is the unit array. Distinguishing the step λ, the eigenvalues of the Hessian matrix are $\lambda_1, \lambda_2, \ldots\ldots$, e, Then, the choice of μ needs to be satisfied

$$\mu + \lambda_i > 0, i = 1, 2 \cdots n \tag{23}$$

i.e.,

$$\mu > \max\{-\lambda_i\} \tag{24}$$

H is modified to remain positive at all times.

The processing flow of the rotational velocity estimation algorithm based on ME-MN is shown in Figure 6.

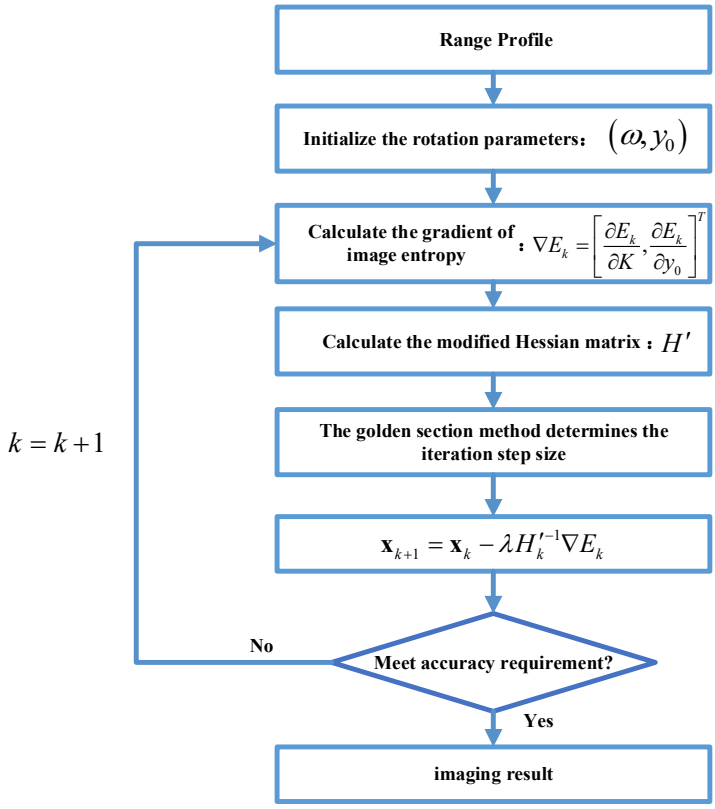

Figure 6. The algorithm processing flowchart.

3.3. Second-Order Space-Varying Range Migration Correction

Through the method in Section 3.2, after the rotational velocity is obtained, the second-order space-varying range migration correction is performed below. Because different scattering point signals are superimposed in the range time domain, it is impossible to compensate the echo with a unified phase to eliminate the second-order range curvature. The frequency is resampled to correct the second-order range curvature by referring to the KT principle. This process can also be realized by CZT transform. The specific implementation process is as follows:

$$S(h,k') = \sum_{n=-N/2}^{N/2-1} S(n,k) \exp[-j2\pi \frac{n}{N}(1 + \frac{1}{2}\omega^2 k'^2 \Delta\tau_m{}^2)h] \tag{25}$$

Finally, Equation (25) can be written as

$$\begin{aligned} S(h;k') = \sum_{i=1}^{Q} \sigma_i \cdot \exp\left[-j\tfrac{4\pi f_c}{c}\left(x_i \omega k' \Delta\tau_m - \tfrac{1}{2} y_i \omega^2 k'^2 \Delta\tau_m{}^2\right)\right] \\ \cdot \sin c\left\{(1 + \tfrac{1}{2}\omega^2 k'^2 \Delta\tau_m{}^2)\left[h + \tfrac{2B}{c} y_i\right]\right\} \end{aligned} \tag{26}$$

The above equation is compensated for the quadratic phase and then an azimuthal FFT is performed. The final imaging result is obtained.

4. Result and Analysis

This section uses the point scattering model simulation data and the complex scattering model electromagnetic calculation data to verify the effectiveness of the proposed THz-ISAR imaging algorithm and processing flow. Firstly, three scattering points are simulated to demonstrate the existence of serious SRM phenomenon in the terahertz frequency band, as well as the effects of SRM and second-order spatially varying phase errors on imaging. Then, the validity of the algorithm is verified based on the point cloud scattering model of the BeiDou satellite and electromagnetic calculation data. At the same time, it is compared with several different algorithms. The superiority of the algorithm is verified.

4.1. Three Scattering Point Simulation Experiments

In this section, three points of simulation data are used for experiments. Table 1 shows the simulation parameters. The positions of the three scattering points are (18 m, 18 m), (−18 m, −18 m), and (−3 m, −3 m). The echo is generated by the signal model in Section 2. The following figures show the range profile after range compression (RDA), the range profile after KT transformation (RDK), and the range profile after second-order space-varying range migration correction, respectively.

Table 1. Parameter setting.

Simulation Parameter	Value
Center frequency	216 GHz
Bandwidth	20 GHz
Pulse repetition frequency	6000 Hz
Rotational velocity	0.1 rad/s
Range-dimension sampling points	6000
Pulse number	6000
Range resolution Radar slant range	0.075 m% 50 km

Figure 7a shows that the traditional RDA does not consider the rotation-induced range migration, and the envelope is severely offset. The migration can reach hundreds of range resolution units, which must be corrected. As shown in Figure 7b, the FRM is corrected by the KT transform, and the envelope alignment is significantly improved. However, the residual SRM causes some bending of the envelope. The bending degree becomes more and more severe as the distance from the rotation center increases. Figure 7c is the range profile after SRM correction, and the envelopes are completely aligned. Envelope alignment is generally measured by envelope sharpness. Envelope sharpness formula:

$$Envelope\ sharpness = \sum_{n=-N/2}^{N/2-1} \left[\sum_{k=-M/2}^{M/2-1} |S(n,k)| \right]^2 \tag{27}$$

where $S(n,k)$ is the range profile. The larger the envelope sharpness, the better the alignment effect. Table 2 shows the comparison of the envelope sharpness of the three range profiles in Figure 7. After correction for FRM by KT transform, envelope sharpness is significantly improved. Similarly, the envelope sharpness is significantly improved after correcting for SRM with the proposed method. This also suggests that THZ-ISAR must take into account the correction for second-order range offsets. After applying the azimuthal Fourier transform to the range profiles, the imaging results are obtained as follows in Figure 8.

Table 2. Parameter setting.

	Original Envelope	After Correction for FRM	The Proposed Method
Envelope sharpness	2.77	8.70	9.80

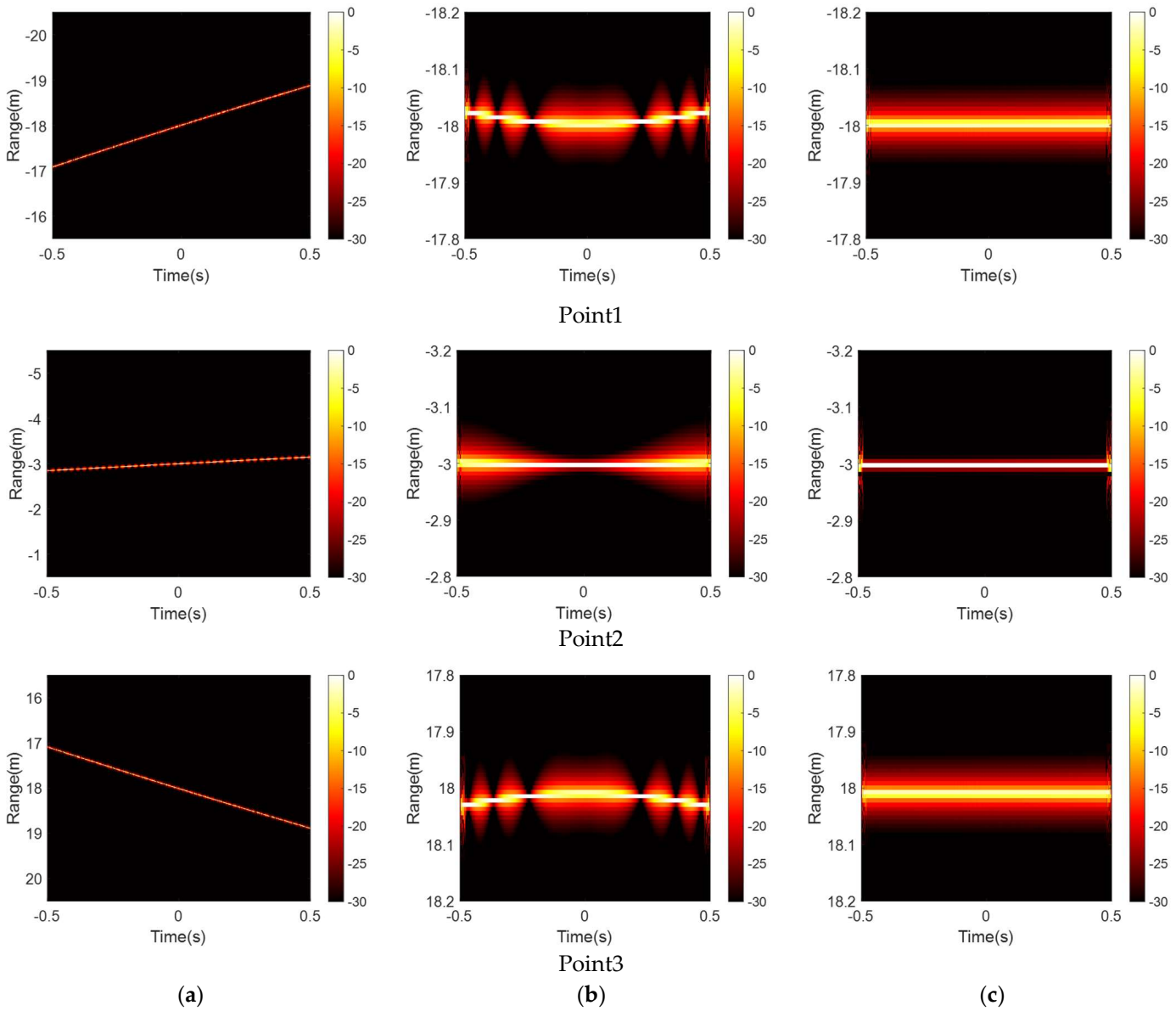

Figure 7. The range profile of three points. (**a**) No range migration correction; (**b**) after FRM correction (**c**) after correction by the method proposed.

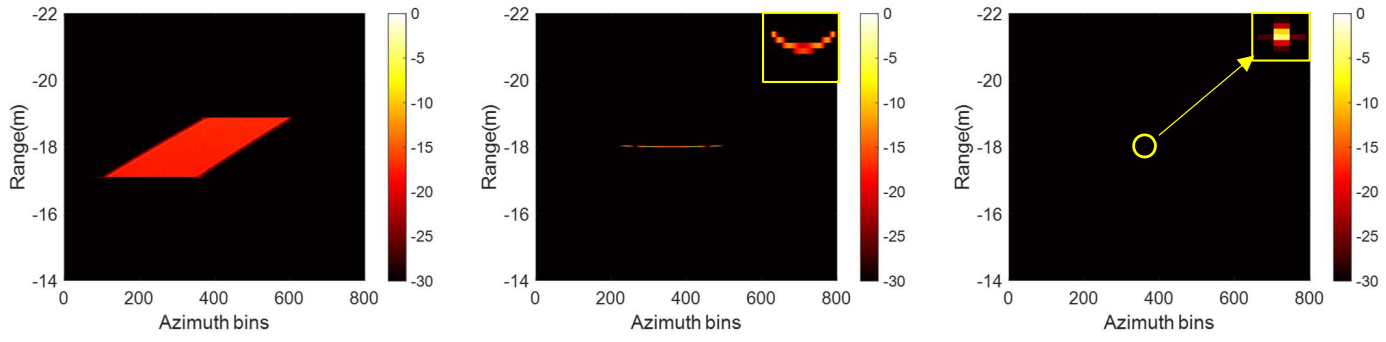

Figure 8. *Cont.*

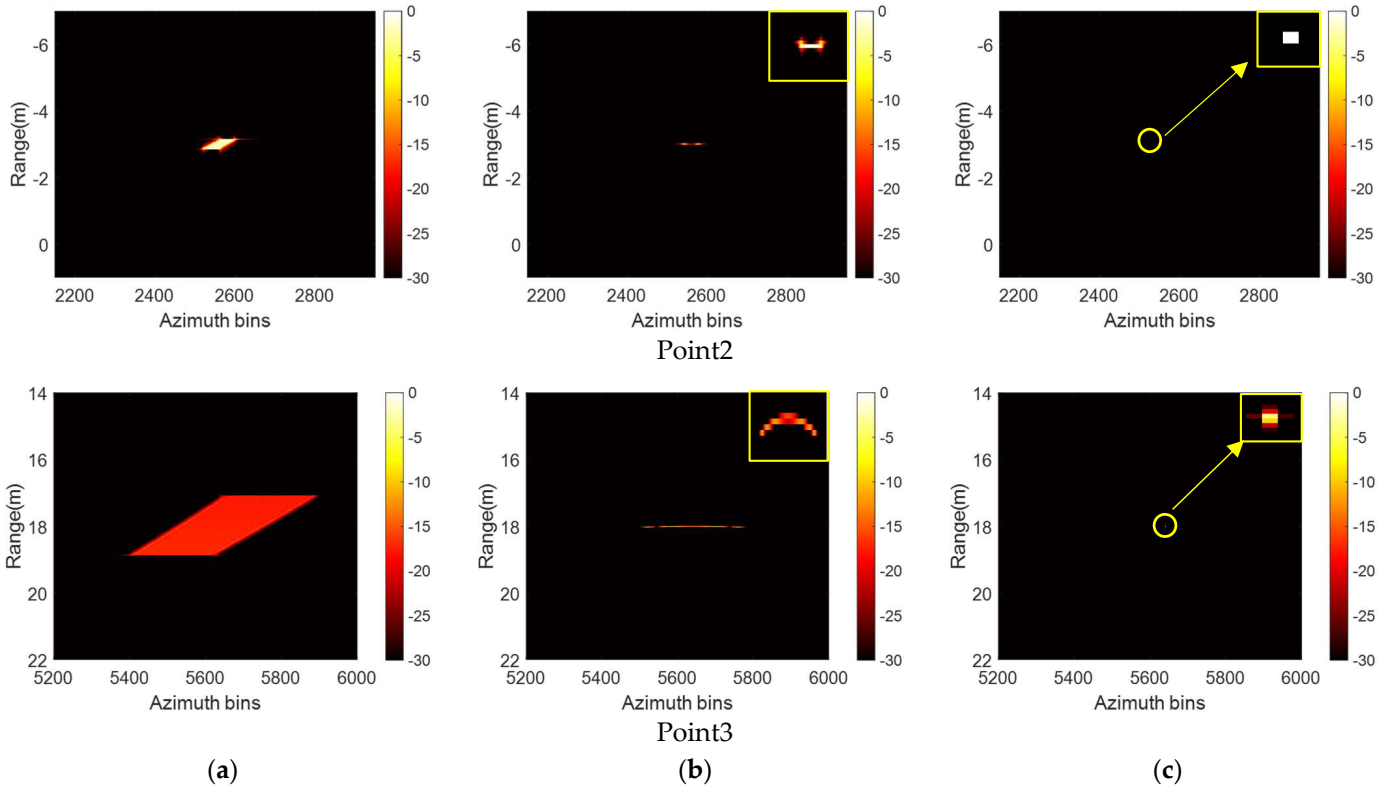

Figure 8. Imaging results of three scattering points. (**a**) No range migration correction; (**b**) after FRM correction (**c**) after correction by the method proposed.

Figure 8 shows the imaging results for the three scattering points. The conventional RDA does not compensate for the distance migration and phase errors, resulting in severe defocus in both the range and azimuth dimensions. And the further away from the rotation center, the more serious the defocus is. The imaging results of point 2 are still severely defocused, indicating that the rotation compensation of small-sized targets is also necessary for the THz band. After FRM correction, although the defocus of the range dimension has been improved to some extent, due to the influence of the second-order range space-varying phase, defocus will still appear in the azimuth dimension. Figures 8b and 9 show that SRM leads to envelope bending and two spikes in the azimuthal profile. Figure 8c shows the imaging results of the proposed method. The scattering points are well-focused. This paper uses image entropy (IE), and image contrast (IC) to measure the imaging effect. The comparison results of the proposed method with the traditional RDA and RDK are shown in Table 3. The proposed algorithm has minimum IE and maximum IC.

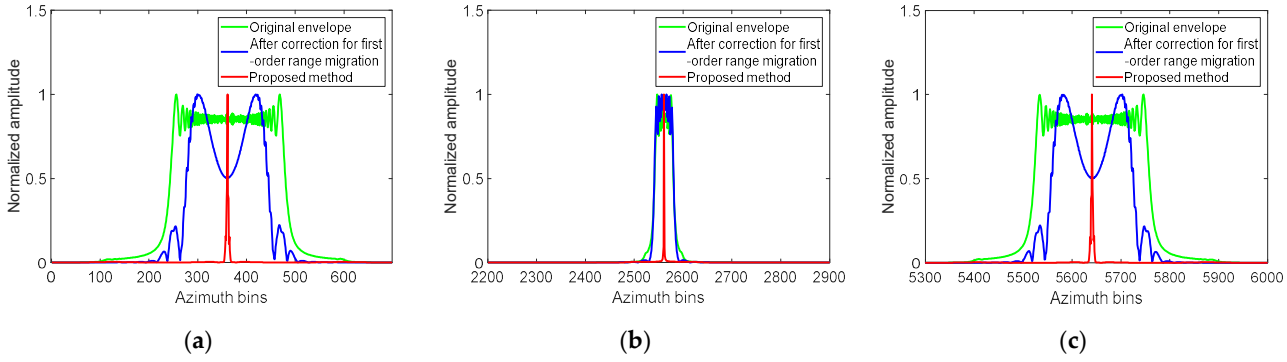

Figure 9. Azimuth profile comparison of three points imaging results. (**a**) Point 1; (**b**) Point 2; (**c**) Point 3.

Table 3. IE and IC of imaging results are in Figure 8.

	Original Envelope	After Correction for FRM	The Proposed Method
IE	10.97	7.06	3.98
IC	50.52	290.07	1.74×10^3

4.2. Beidou Satellite Point Cloud Model Simulation Experiments

In this section, the Beidou satellite model composed of point clouds shown in Figure 10 is used to generate experimental data. And the proposed method is compared with RDA, RDK, and PFA. The PFA algorithm is a method of mapping data from polar coordinates to right-angle coordinates using interpolation. The method is effective in correcting range migration and phase errors but requires accurate corner information. The main radar parameters are consistent with the settings in Section 4.2, and the number of model point clouds is about 112,000. The obtained envelope image and zoom-in image results are shown in Figures 10 and 11. Since the PFA algorithm achieves imaging by interpolation, its envelope is not compared to other algorithms.

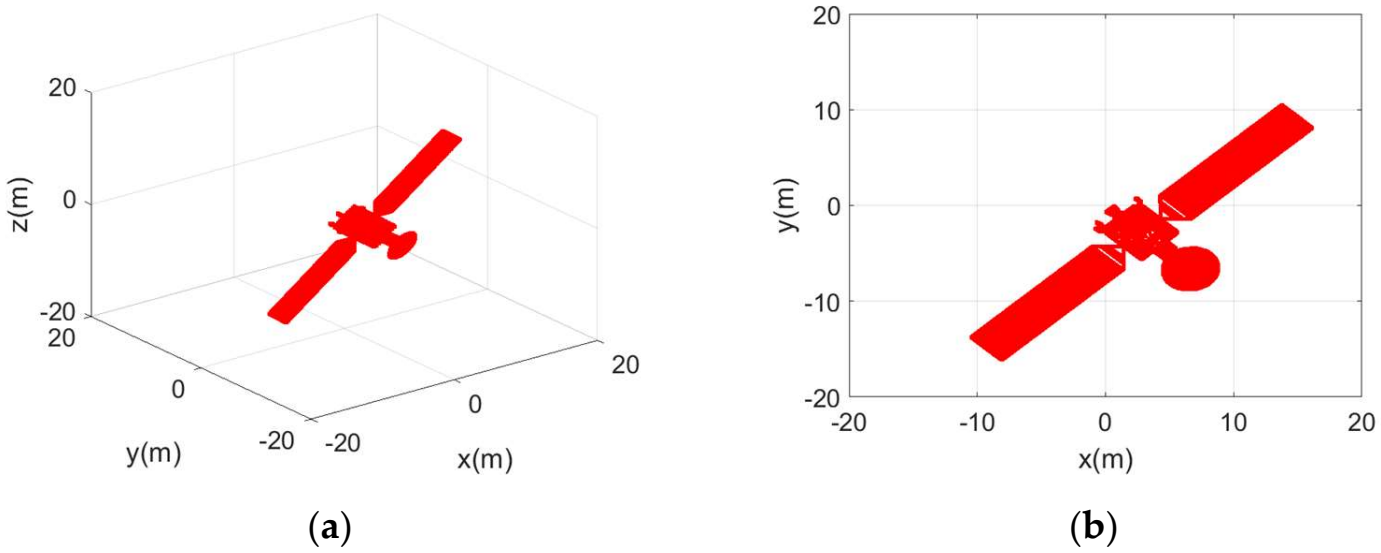

Figure 10. Point cloud model of Beidou satellite. (**a**) 3D model; (**b**) 2D model.

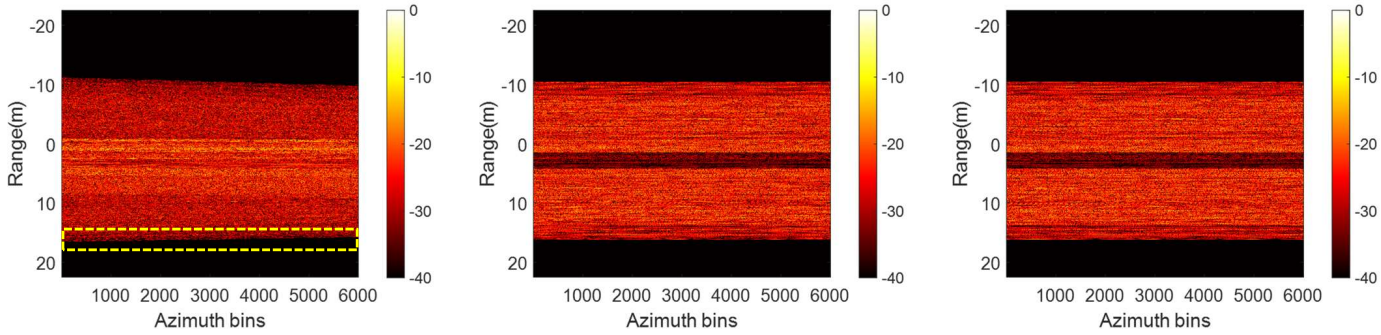

Figure 11. *Cont.*

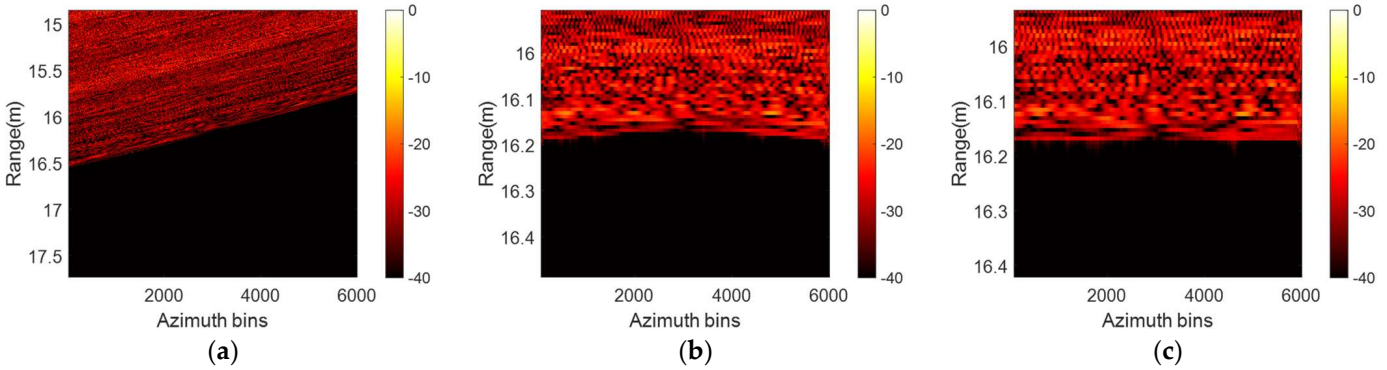

Figure 11. Envelope image and zoom-in image results obtained by the three algorithms. (**a**) RDA; (**b**) RDK; (**c**) the proposed method.

Figure 11a shows the envelope image and zoom-in image result of RDA. The final imaging results obtained are shown in Figure 12a,b. Since the traditional RDA ignores the range offset generated by the target motion, the envelope image is severely shifted. The obtained imaging results produce severe defocus both in whole and locally. As shown in Figure 11b, the range migration is partially corrected after the KT. From Figure 12c,d, it can be seen that the imaging result of the central local area is improved, but some details are lost. The further away from the central part, the more serious the defocus is. Figure 12e,f show the PFA imaging results. The PFA algorithm requires the target's rotational velocity information. Here, we use the error-free rotational velocity for PFA imaging. The results show that the PFA algorithm is better compared to the RDA and RDK for imaging. However, the PFA algorithm requires interpolation operation and slower arithmetic in the process of implementation. Moreover, for THz radar, the ability of the PFA algorithm to correct the range migration is limited, and the imaging effect is very good for the region with a small migration offset, but for the region with a large migration, it still generates defocusing. The range profile and imaging results obtained by the proposed method are shown in Figures 11c and 12g,h. The rotational velocity calculated by the proposed algorithm is 0.1025 rad/s, and the error with the actual rotational velocity estimation is 2.5%. A well-aligned range profile envelope is obtained, and the imaging results are superior to the above three methods. At the same time, the details of the imaging results are more prominent, reflecting the advantages of high resolution of THz radar imaging. Table 4 shows the IE and IC of the four algorithms. The results show that our method has better imaging results.

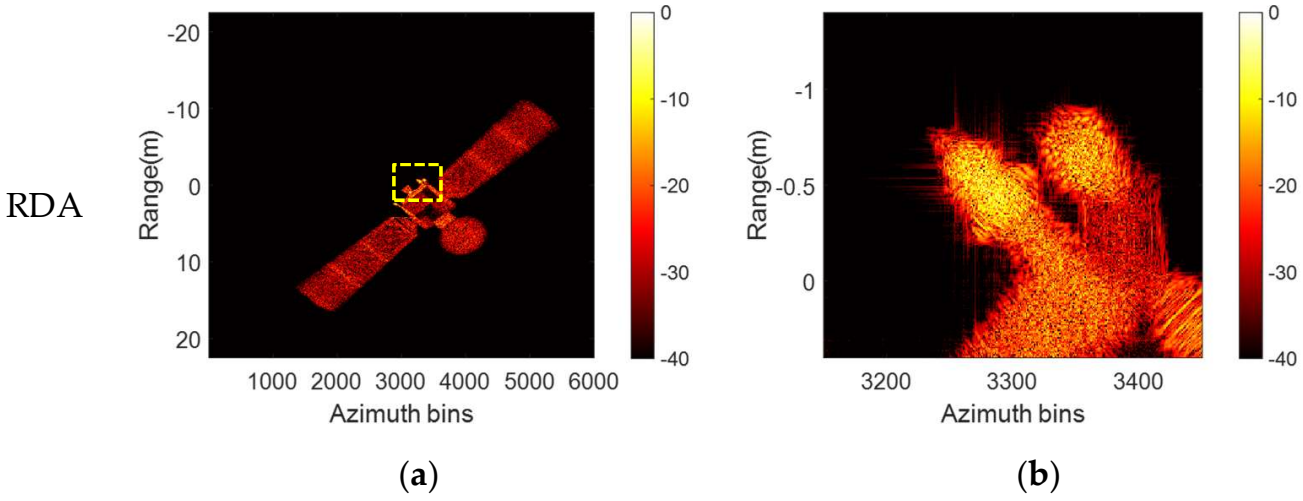

Figure 12. *Cont.*

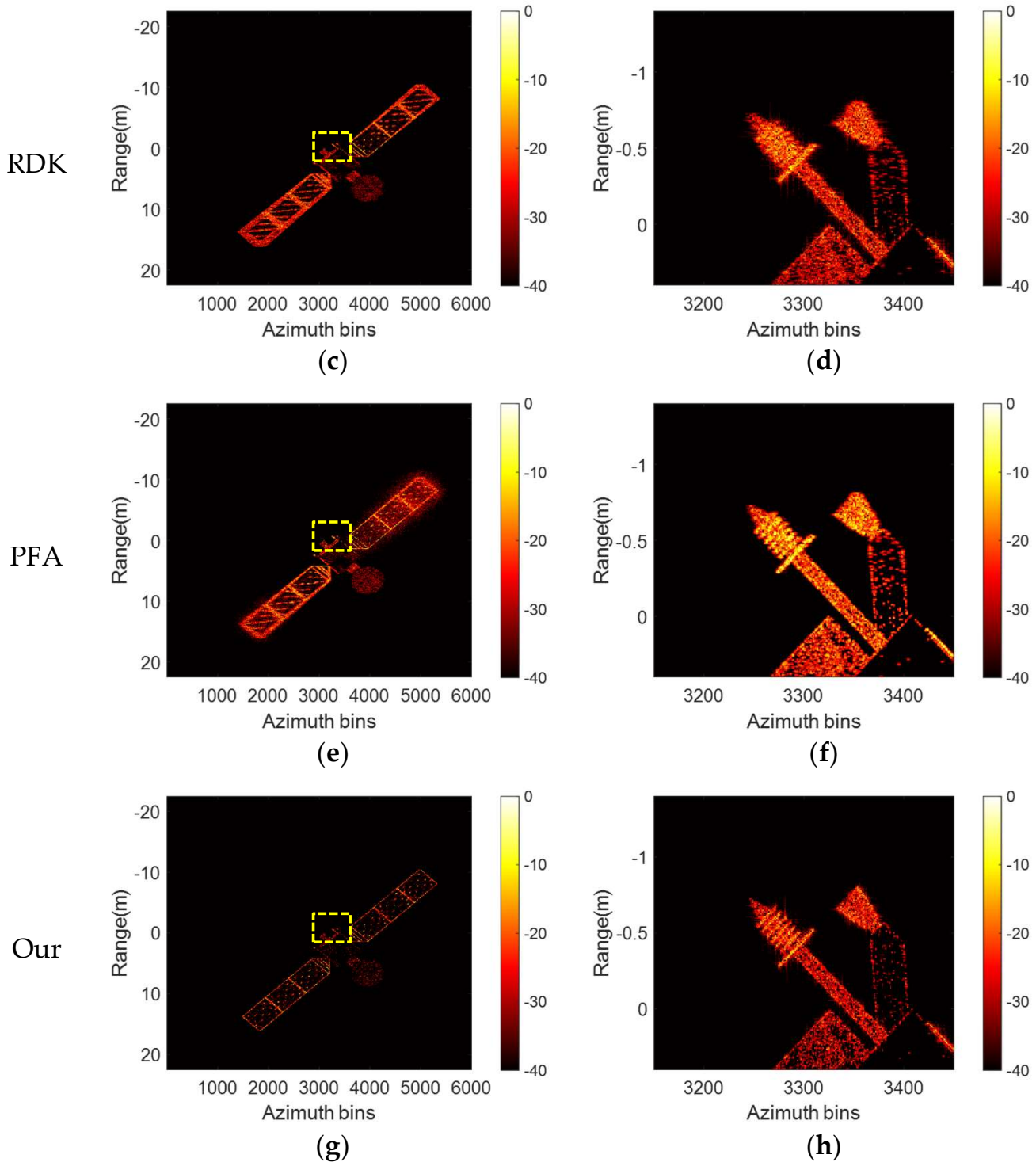

Figure 12. Imaging and zoom-in image results were obtained by the four algorithms. (**a**,**b**) RDA. (**c**,**d**) RDK; (**e**,**f**) PFA; (**g**,**h**) the proposed method.

Table 4. IE and IC of imaging results in Figure 12.

	RDA	RDK	PFA	The Proposed Method
IE	14.07	13.37	13.44	11.83
IC	10.37	11.80	12.66	24.93

Figure 13 is the iterative curve based on NE-NM. In Figure 13, the convergence is achieved after seven iterations, indicating that the NM has a faster convergence speed. Since the rotational parameters estimated by the Newton iteration method for the first time are very close to the true value, the second ME-MN takes the result of the first ME-MN as the initial value, and the second ME-MN converges after only one iteration.

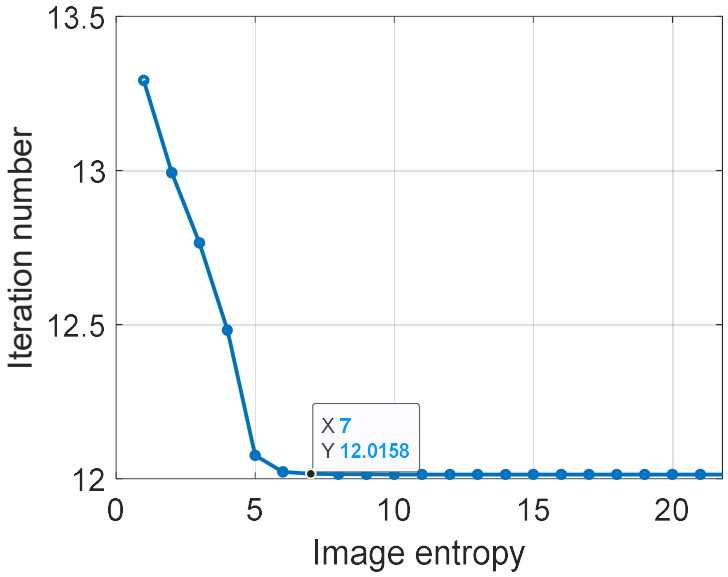

Figure 13. Iterative curve.

4.3. Beidou Satellite Electromagnetic Simulation Experiment

In Section 4.3, the validity of the algorithm is verified with the electromagnetic computational data. The model adopts the BeiDou satellite model. In this paper, the maximum size of the model is set to be about 9 m. Because of the short wavelength of the terahertz band, the model belongs to the super-electric large-size model, and the computational complexity is huge. The parameters are set as follows: the frequency range is 206~226 GHz, the frequency step is 16.7 MHz, the observation angle is—6°~6°, and the angle interval is 0.006°.

Figure 14 shows the range profile obtained by the three algorithms with local zoom results, which are consistent with the conclusions obtained from the simulation in Section 4.2. The RDA and RDK produce serious range migration. While the range profile obtained by the proposed method is shown in Figure 14c, the envelope has been better aligned. Figure 15 shows the imaging results obtained by the four algorithms with local zoom. The results of the RDA are shown in Figure 15a–c. Owing to the effects of range migration and phase error, the imaging results show that the straight edges of the satellite's solar sail panels produce severe bending and trailing, and the dot matrix on the solar sail panels demonstrates severe defocus, making it difficult to identify the target. The results of the RDK are shown in Figure 15d–f. The bending of some linear structures on the satellite is improved compared to the RDA, but the defocus still exists. Figure 15g–i shows the results of PFA. The imaging results are more focused compared to RDA and RDK. And PFA corrects the range migration and Doppler migration by interpolation. However, its ability to correct is limited, and its imaging results deteriorate when the amount of migration exceeds a certain amount. The results of the proposed algorithm are shown in Figure 15j–i. Compared with the previous three algorithms, the proposed method can recover some linear structures on the satellite better. Meanwhile, the IE and IC of these algorithms are shown in Table 5. The results also show that the proposed method has a better imaging effect.

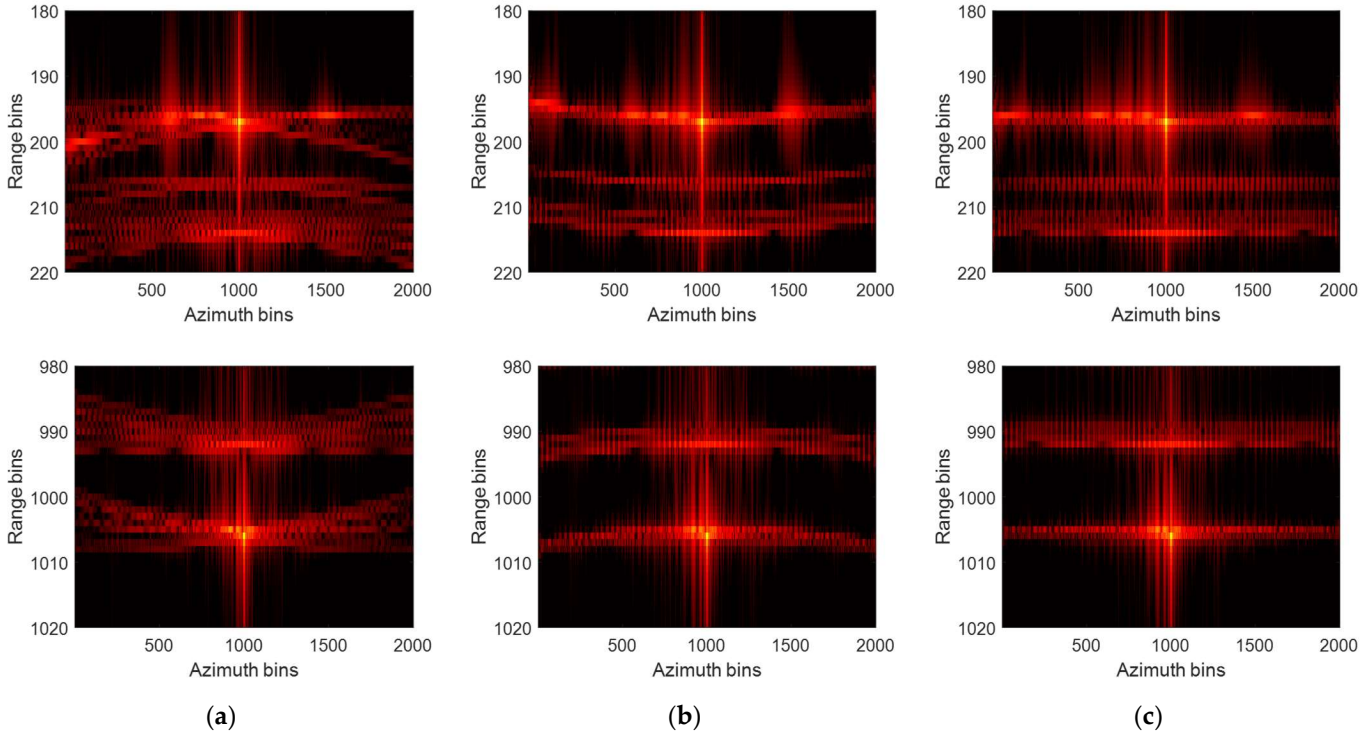

Figure 14. Envelope zoom-in imaging results of one-dimensional range profile; (**a**) RDA; (**b**) RDK; (**c**) the proposed method.

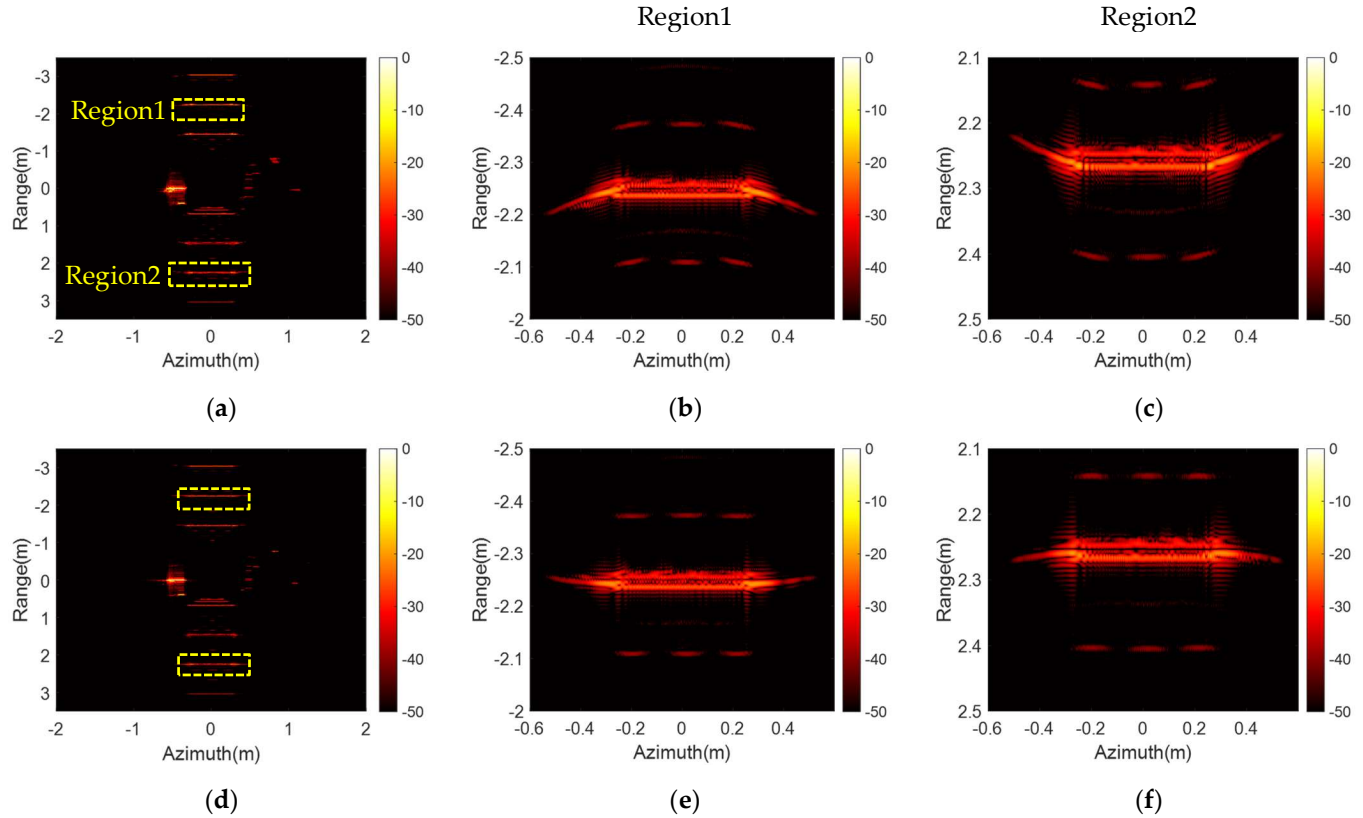

Figure 15. *Cont.*

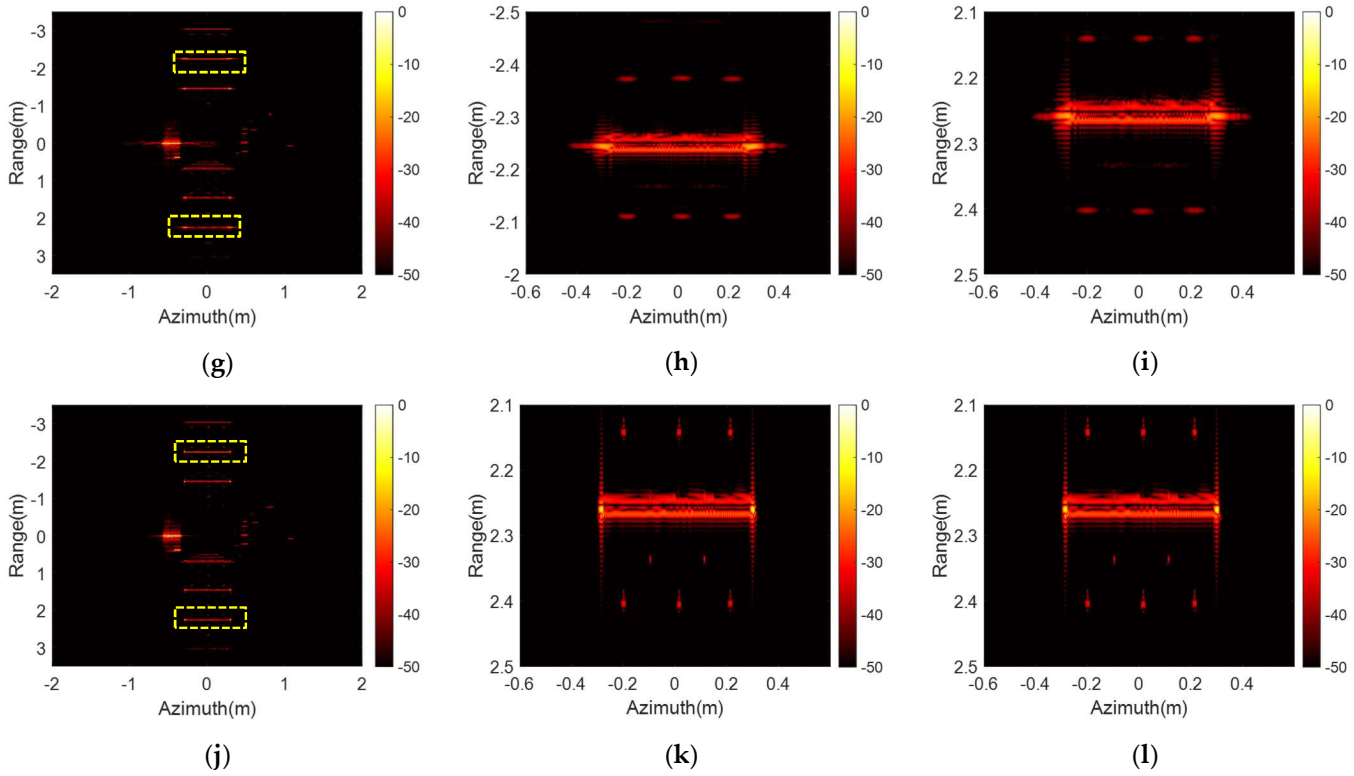

Figure 15. The imaging results and local enlarged images of three methods (**a**–**c**) RDA; (**d**–**f**) RDK; (**g**–**i**) PFA; (**j**–**l**) the proposed method.

Table 5. IE and IC of imaging results in Figure 15.

	RDA	RDK	PFA	The Proposed Method
IE	11.13	10.92	10.96	10.81
IC	109.38	116.16	116.78	118.00

To verify the robustness of the algorithms, we conducted experiments under different SNR conditions. Figure 16 illustrates the results of the four imaging algorithms under the conditions of SNRs of −5 dB, 0 dB, 5 dB, and 10 dB, respectively. Figure 17a,b are the results of the rotational velocity estimation and the relative error with the true value, respectively. Figure 17c is the contrast curve of the IE of the four algorithms under different SNRs. It can be found that our method has better results at different SNRs.

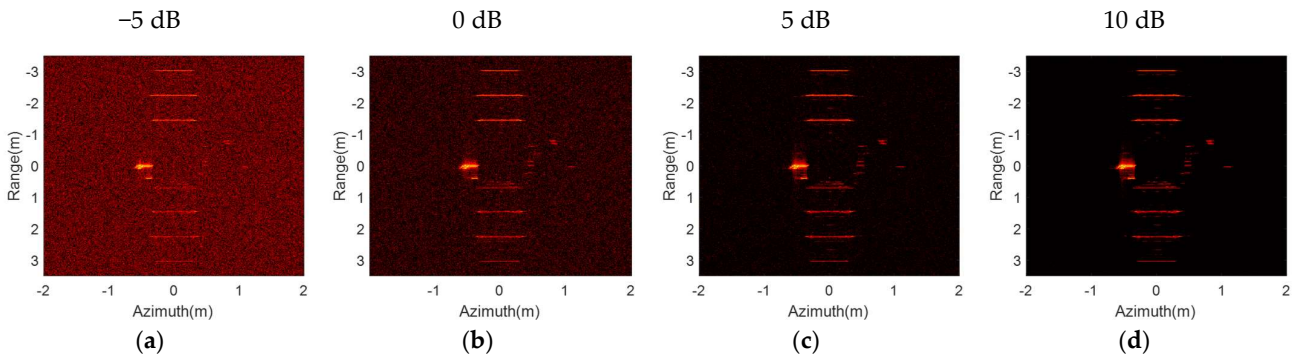

Figure 16. *Cont.*

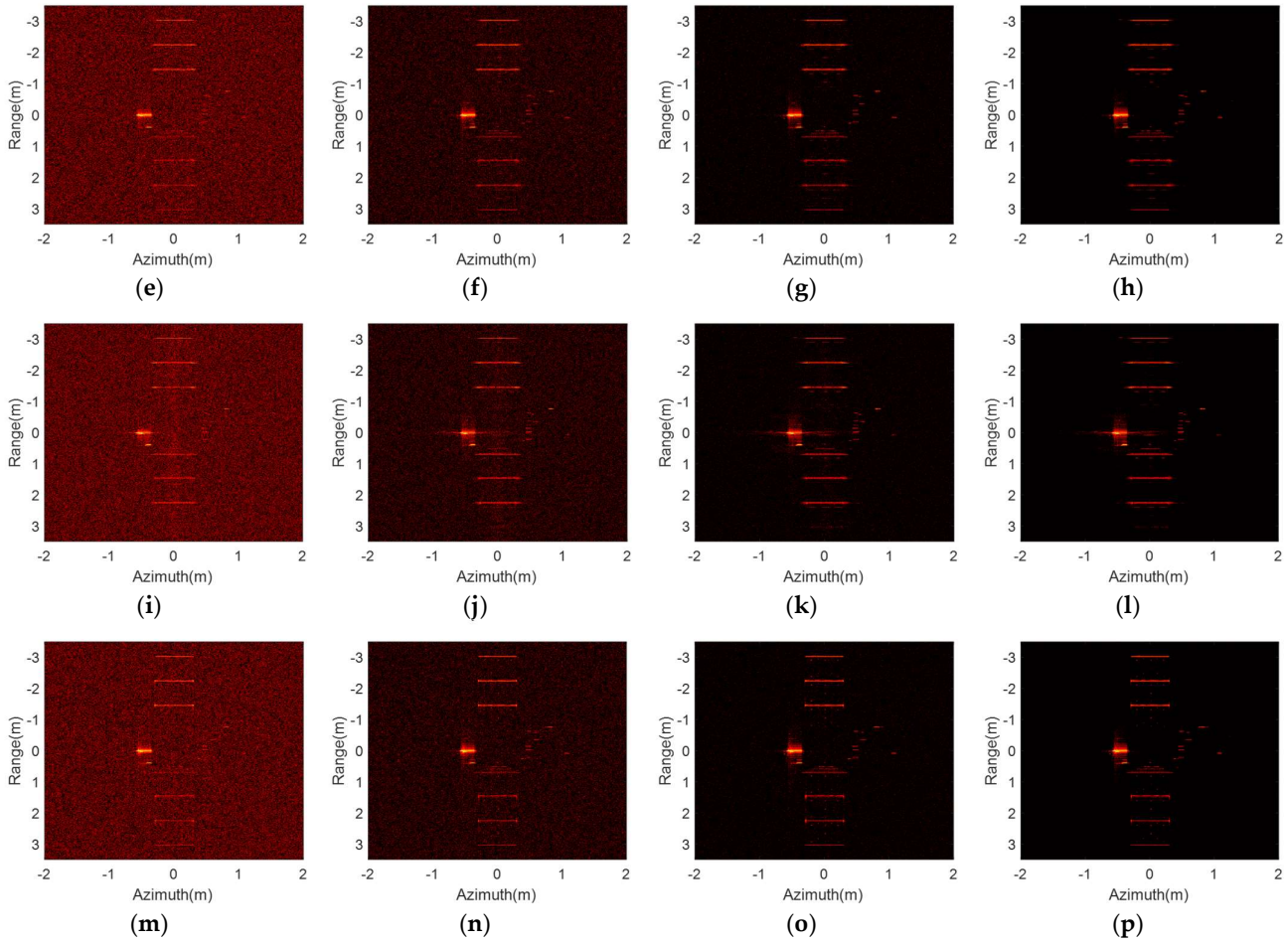

Figure 16. The imaging results of three algorithms under different SNRs (the SNR is 10 dB, 5 dB, 0 dB, −5 dB, respectively). (**a**–**d**) RDA; (**e**–**h**) RDK; (**i**–**l**) PFA; (**m**–**p**) the proposed method.

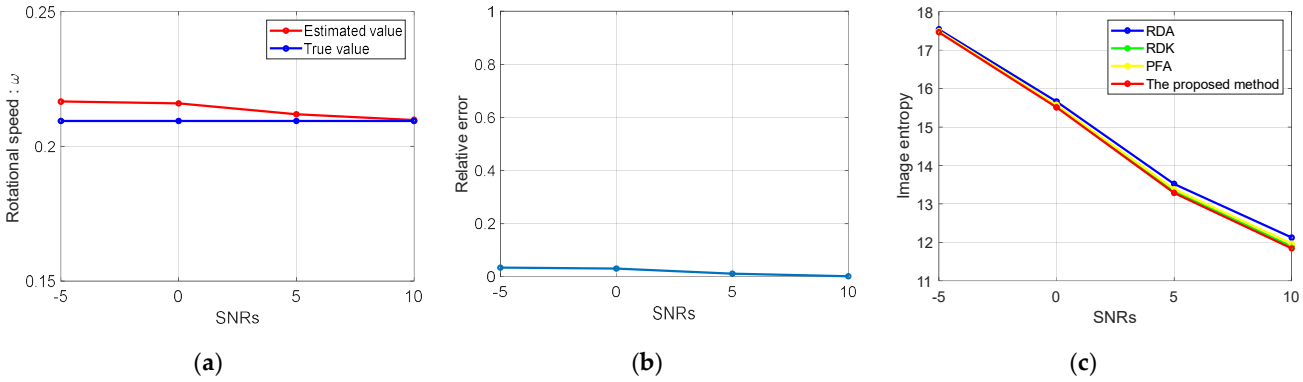

Figure 17. (**a**) The rotational velocity estimation results under different SNRs. (**b**) Relative error of rotational velocity estimation under different SNRs. (**c**) IE of four algorithms under different SNRs.

5. Conclusions

The range migration and high-order phase error caused by rotation in THz-ISAR imaging seriously affect the ISAR imaging results, resulting in serious image blurring. This paper proposes a THz-ISAR algorithm. Firstly, the method corrects the FRM through the KT. Then, the NE-MN is used twice to accurately estimate the rotational velocity, and correct the SRM by CZT to avoid the influence of the range migration coupling on the rotational velocity estimation. Finally, compensate for the phase error to obtain well-focused results. Both simulation data and electromagnetic calculation data verify the effectiveness

of the algorithm. Experiments under different SNR conditions verify the robustness of the algorithm. In addition to obtaining ultra-high-resolution imaging results with THz radar, there are other issues worth investigating. The main directions and contents of our future research are:

(1) THz radar target characterization. Due to the short wavelength of terahertz radar, some special structures of the target such as cavities, and dihedral angles show different characteristics in imaging. This is also a very worthwhile direction.
(2) The imaging results are defocused due to some special structures on the target such as cavities. And this part of the defocusing will affect the image entropy very drastically, which leads to the wrong estimation of rotational velocity and makes it difficult to get accurate results. In the future, we will consider adopting local entropy as the image quality evaluation indicator, to avoid the influence of some special structures on the target. Similarly, how to adaptively select effective local regions is also a very important work.
(3) Due to the reason of limited detection range of THz radar, the research object considered in this paper is the space target. And the problem of applying THz radar to space platforms to detect and image space targets involves multidisciplinary intersection. How to carry out the design of space track and imaging strategy needs to be further studied.

Author Contributions: Theoretical study, experiments, and writing W.L.; experimental environment and software H.W. and B.D.; review and editing, L.F., J.Y. and Q.Y. All authors have read and agreed to the published version of the manuscript.

Funding: This work was supported by the National Key R&D Program of China under Grand 2022YFB3902400 and Grand 2018YFB2202500, the National Natural Science Foundation of China under Grant 62201591, Grant 62035014, Grant 61921001, and Grant 61971427.

Data Availability Statement: Not applicable.

Acknowledgments: The authors extend their sincere thanks to the editors and reviewers for their careful reading and fruitful suggestions.

Conflicts of Interest: The authors declare no conflict of interest.

References

1. Shao, S.; Liu, H.; Zhang, L.; Wang, P.; Wei, J. Ultrawideband ISAR Imaging of Maneuvering Targets With Joint High-Order Motion Compensation and Azimuth Scaling. *IEEE Trans. Geosci. Remote Sens.* **2022**, *60*, 5214621. [CrossRef]
2. Walker, J.L. Range-Doppler Imaging of Rotating Objects. *IEEE Trans. Aerosp. Electron. Syst.* **1980**, *AES16*, 23–52. [CrossRef]
3. Fan, H.; Ren, L.; Mao, E.; Liu, Q. A High-Precision Method of Phase-Derived Velocity Measurement and Its Application in Motion Compensation of ISAR Imaging. *IEEE Trans. Geosci. Remote Sens.* **2018**, *56*, 60–77. [CrossRef]
4. Mostajeran, A.; Naghavi, S.M.; Emadi, M.; Samala, S.; Ginsburg, B.P.; Aseeri, M.; Afshari, E. A High-Resolution 220-GHz Ultra-Wideband Fully Integrated ISAR Imaging System. *IEEE Trans. Microw. Theory Tech.* **2019**, *67*, 429–442. [CrossRef]
5. Zhang, Y.; Yang, Q.; Deng, B.; Qin, Y.; Wang, H. Experimental Research on Interferometric Inverse Synthetic Aperture Radar Imaging with Multi-Channel Terahertz Radar System. *Sensors* **2019**, *19*, 2330. [CrossRef] [PubMed]
6. McIntosh, R.E.; Narayanan, R.M.; Mead, J.B.; Schaubert, D.H. Design and Performance of a 215-Ghz Pulsed Radar System. *IEEE Trans. Microw. Theory Tech.* **1988**, *36*, 994–1001. [CrossRef]
7. Cooper, K.B.; Dengler, R.J.; Llombart, N.; Thomas, B.; Chattopadhyay, G.; Siegel, P.H. THz Imaging Radar for Standoff Personnel Screening. *IEEE Trans. Terahertz Sci. Technol.* **2011**, *1*, 169–182. [CrossRef]
8. Gu, S.; Li, C.; Gao, X.; Sun, Z.; Fang, G. Three-dimensional image reconstruction of targets under the illumination of terahertz gaussian beam-theory and experiment. *IEEE Trans. Geosci. Remote Sens.* **2013**, *51*, 2241–2249. [CrossRef]
9. Liu, T.; Pi, Y.; Yang, X. Wide-Angle CSAR Imaging Based on the Adaptive Subaperture Partition Method in the Terahertz Band. *IEEE Trans. Terahertz Sci. Technol.* **2018**, *8*, 165–173. [CrossRef]
10. Kim, S.-H.; Fan, R.; Dominski, F. ViSAR: A 235 GHz Radar for Airborne Applications. ["Advanced Concepts and Technology, Raytheon, Space and Airborne Systems, El Segundo, CA"]. In Proceedings of the 2018 IEEE Radar Conference (RadarConf18), Oklahoma City, OK, USA, 23–27 April 2018.
11. Marchetti, E.; Stove, A.G.; Hoare, E.G.; Cherniakov, M.; Blacknell, D.; Gashinova, M. Space-Based Sub-THz ISAR for Space Situational Awareness—Concept and Design. *IEEE Trans. Aerosp. Electron. Syst.* **2022**, *58*, 1558–1573. [CrossRef]

12. Marchetti, E.; Stove, A.G.; Hoare, E.G.; Cherniakov, M.; Blacknell, D.; Gashinova, M. Space-Based Sub-THz ISAR for Space Situational Awareness—Laboratory Validation. *IEEE Trans. Aerosp. Electron. Syst.* **2022**, *58*, 4409–4422. [CrossRef]
13. Marchetti, E.; Stove, A.; Hoare, E.; Cherniakov, M.; Gashinova, M. Images of satellite elements with a space-borne Sub-THz ISAR system. In Proceedings of the 2021 18th European Radar Conference (EuRAD), London, UK, 5–7 April 2022.
14. Chen, C.-C.; Company, H.A.; Andrews, H.C. Target-Motion-Induced Radar Imaging. *IEEE Trans. Aerosp. Electron. Syst.* **1980**, *AES16*, 2–14. [CrossRef]
15. Zhu, D.; Wang, L.; Yu, Y.; Tao, Q.; Zhu, Z. Robust ISAR Range Alignment via Minimizing the Entropy of the Average Range Profile. *IEEE Geosci. Remote Sens. Lett.* **2009**, *6*, 204–208. [CrossRef]
16. Wu, H.; Grenier, D.; Delisle, G.; Fang, D. Translational motion compensation in ISAR image processing. *IEEE Trans. Image Process.* **1995**, *4*, 1561–1571. [CrossRef] [PubMed]
17. Kim, K.S.; Yang, E.J.; Kim, C.H.; Park, S.C. Improvement of ISAR Autofocusing Performance Based on PGA. *J. Korea Inst. Mil. Sci. Technol.* **2014**, *17*, 680–687. [CrossRef]
18. Xi, L.; Guosui, L.; Ni, J. Autofocusing of ISAR images based on entropy minimization. *IEEE Trans. Aerosp. Electron. Syst.* **1999**, *35*, 1240–1252. [CrossRef]
19. Berizzi, F.; Corsini, G. Autofocusing of inverse synthetic aperture radar images using contrastoptimization. *IEEE Trans. Aerosp. Electron. Syst.* **1996**, *32*, 1185–1191. [CrossRef]
20. Sun, G.; Xing, M.; Xia, X.; Wu, Y.; Bao, Z. Robust ground moving-target imaging using deramp-keystone processing(Article). *IEEE Trans. Geosci. Remote Sens.* **2013**, *51*, 966–982. [CrossRef]
21. Yang, L.; Xing, M.; Zhang, L.; Sun, G.-C.; Gao, Y.; Zhang, Z.; Bao, Z. Integration of Rotation Estimation and High-Order Compensation for Ultrahigh-Resolution Microwave Photonic ISAR Imagery. *IEEE Trans. Geosci. Remote Sens.* **2021**, *59*, 2095–2115. [CrossRef]
22. Wang, H.; Yang, Q.; Wang, H.; Deng, B. Autofocusing of Maneuvering Targets in Terahertz Inverse Synthetic Aperture Radar Imaging Based on Damped Newton Method. *Sensors* **2022**, *22*, 6883. [CrossRef]
23. Li, Z.; Xing, M.; Xing, W.; Liang, Y.; Gao, Y.; Dai, B.; Hu, L.; Bao, Z. A Modified Equivalent Range Model and Wavenumber-Domain Imaging Approach for High-Resolution-High-Squint SAR with Curved Trajectory. *IEEE Trans. Geosci. Remote Sens.* **2017**, *55*, 3721–3734. [CrossRef]
24. Zhang, S.; Liu, Y.; Li, X.; Bi, G. Fast ISAR Cross-range Scaling Using Modified Newton Method. *IEEE Trans. Aerosp. Electron. Syst.* **2018**, *54*, 1355–1367. [CrossRef]